Resistive magnetohydrodynamics Simulation of Fusion Plasmas *

***X.Z. Tang*[†], *G.Y. Fu*[‡], *S.C. Jardin*[§], *L.L. Lowe*[¶], *W. Park*[‖] *and H.R. Strauss*[**]**

1 Introduction

Although high-temperature plasmas in laboratory magnetic fusion confinements are sufficiently collisionless that formal fluid closures are difficult to attain, the resistive MHD model has proven, by comparison with experimental data, to be useful for describing the large scale dynamics of magnetized plasmas [1]. Resistive MHD model consists of Faraday's law for the evolution of the magnetic field and Navier-Stokes equation for the plasma flow. These equations are closed by the Ohm's law and an equation of state for the plasma.

$$\frac{\partial \mathbf{B}}{\partial t} = -\nabla \times \mathbf{E}; \tag{1}$$

$$\mathbf{E} = -\mathbf{v} \times \mathbf{B} + \eta \mathbf{J}; \tag{2}$$

$$\rho \frac{d\mathbf{v}}{dt} = \mathbf{J} \times \mathbf{B} - \nabla p + \rho \nu \nabla^2 \mathbf{v}; \tag{3}$$

$$\frac{\partial \rho}{\partial t} = -\nabla \cdot (\rho \mathbf{v}); \tag{4}$$

*This work was supported by U.S. Department of Energy
[†]Princeton Plasma Physics Laboratory, xtang@pppl.gov
[‡]Princeton Plasma Physics Laboratory
[§]Princeton Plasma Physics Laboratory
[¶]Department of Physics, Drexel University
[‖]Princeton Plasma Physics Laboratory
[**]New York University

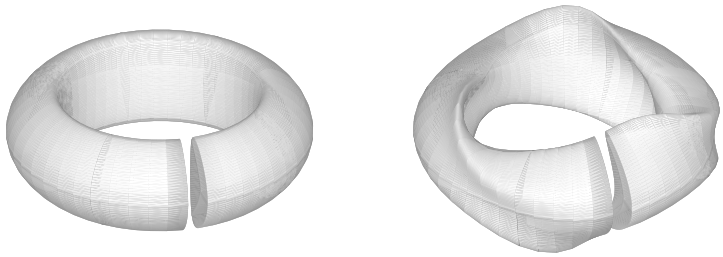

Figure 1. Tokamak (left) has a toroidal axisymmetry, but stellerator (right) does not.

$$\frac{dp}{dt} = -\gamma p \nabla \cdot \mathbf{v} + \rho \nabla \cdot \kappa \cdot \nabla \frac{p}{\rho}, \tag{5}$$

where η is the plasma resistivity, ν is the kinematic viscosity, γ the ratio of specific heats, and κ a tensor thermal conductivity. For a magnetized plasma, heat conduction is usually many orders of magnitude faster along the field line than that across due to charged particles free-streaming along the field lines.

The front runners of magnetic confinements have a toroidal geometry. Devices like Tokamak have toroidal axisymmetry, while stellerators do not, see fig. (1) for an illustration. The purpose of this paper is to present the design and implementation of a resistive MHD code for a general toroidal geometry. This code is targeted for massively parallel distributed memory computers, and constructed in the framework of PETSc [2].

2 Current-Vorticity Formulation

We adopt a mixed field and flux representation for the magnetic field $\mathbf{B}$ following [3],

$$\mathbf{B} = \nabla\psi \times \nabla\varphi + \frac{1}{R}\nabla_\perp F + R_0 I \nabla\varphi, \tag{6}$$

in a cylindrical coordinates (R, Z, φ). The (R, Z) plane at a specified toroidal angle φ is called a poloidal plane, where $\nabla_\perp \equiv \frac{\partial}{\partial R}\hat{R} + \frac{\partial}{\partial Z}\hat{Z}$. The magnetic field is divergence-free so only two of the three functions ψ, F, and I are independent. Applying $\nabla \cdot \mathbf{B} = 0$ to equation (6) one finds

$$\nabla_\perp^2 F = -\frac{R_0}{R} I' \tag{7}$$

with $I' = \partial I / \partial \varphi$.

The plasma flow field also has a mixed field and stream function representation[3],

$$\mathbf{v} = \epsilon R^2 \nabla U \times \nabla\varphi + \nabla_\perp \chi + v_\varphi \hat{\varphi}, \tag{8}$$

with $\epsilon \equiv a/R_0$ the inverse aspect ratio of the torus. We have assumed a compressible plasma so all three functions U, χ, and v_φ are independent. This particular form of flow field representation separates the dominant incompressible part (U) and compressible part (χ) of the flow field. The benefit of this formulation is the separation of the compressible Alfvén dynamics and the incompressible shear Alfvén dynamics, and hence different sets of equations can be treated with different numerical time stepping schemes.

The numerical solver takes on a dimensionless form of the MHD equations. This is done by normalizing the magnetic field with the toroidal field at the magnetic axis, the flow field with the Alfvén speed defined as $v_A \equiv B_0/\sqrt{\rho_0}$, time with a toroidal transit time $\tau_A \equiv R_0/v_A$, length with the minor radius a. The density is also made dimensionless by writing

$$\rho = \rho_0 \frac{R_0^2}{R^2} d.$$

The pressure p is scaled by the magnetic pressure ϵB_0^2. In this dimensionless form, an $1/R$ field can be pulled out of I

$$I = \frac{R}{R_0} B_\varphi = 1 + \epsilon \tilde{I} \tag{9}$$

with the inverse aspect ratio $\epsilon \equiv a/R_0$. Taking the curl of the magnetic field the plasma current is

$$\mathbf{J} = J_\varphi \hat{\varphi} + \nabla \tilde{I} \times \nabla\varphi - \frac{1}{R} \nabla_\perp F' \times \nabla\varphi + \frac{1}{R^2} \nabla_\perp \psi'. \tag{10}$$

Next we define an auxiliary variable C as

$$C \equiv -R J_\varphi = \Delta^* \psi + \frac{1}{R} \frac{\partial F}{\partial Z}.$$

The original MHD equations can be transformed into a set of time evolution equations for $\tilde{I}, \Delta^*\psi, \Delta^\dagger U, v_\varphi, \Delta^*\chi, d$, and p,

$$\begin{aligned}
\frac{\partial \tilde{I}}{\partial t} = & -\epsilon R \hat{\varphi} \cdot \nabla_\perp \tilde{I} \times \nabla_\perp U - R_0 I \Delta^* \chi - \nabla_\perp \tilde{I} \cdot \nabla_\perp \chi \\
& + R\hat{\varphi} \cdot [\nabla(\frac{v_\varphi}{R}) \times \nabla_\perp \psi] - \frac{v_\varphi}{R} \frac{\partial \tilde{I}}{\partial \varphi} + R \nabla_\perp F \cdot \nabla_\perp (\frac{v_\varphi}{R}) \\
& + \nabla_\perp \eta \cdot \nabla_\perp \tilde{I} - \frac{1}{R} \nabla_\perp \eta \cdot \nabla_\perp F' - \frac{1}{R} (\nabla_\perp \eta \times \nabla_\perp \psi') \cdot \hat{\varphi} \\
& + \eta [\Delta^* \tilde{I} + \frac{1}{R^2} \frac{\partial^2 \tilde{I}}{\partial \varphi^2} + \frac{2}{R^2} (\frac{\partial F'}{\partial R} + \frac{\partial \psi'}{\partial Z})]
\end{aligned} \tag{11}$$

$$\nabla_\perp^2 F = -\tilde{I}'/R \tag{12}$$

$$\begin{aligned}
\frac{\partial}{\partial t}\Delta^*\psi = & \frac{R}{R_0}\{\nabla_\perp U \times \nabla_\perp(\Delta^*\psi)\cdot\hat{\varphi} + \nabla_\perp(\Delta^\dagger U)\times\nabla_\perp\psi\cdot\hat{\varphi} \\
& +2\nabla_\perp\frac{\partial U}{\partial R}\times\nabla_\perp\frac{\partial\psi}{\partial R}\cdot\hat{\varphi} + 2\nabla_\perp\frac{\partial U}{\partial Z}\times\nabla_\perp\frac{\partial\psi}{\partial Z}\cdot\hat{\varphi}\} \\
& +2\epsilon\nabla_\perp U\times\nabla_\perp\frac{\partial\psi}{\partial R}\cdot\hat{\varphi} + 2\frac{\epsilon}{R}\frac{\partial\psi}{\partial R}\frac{\partial U}{\partial Z} \\
& +\frac{R}{R_0}\{-\frac{1}{R}\nabla_\perp U\cdot\nabla_\perp\frac{\partial\tilde{I}}{\partial\varphi} + \frac{1}{R^2}\frac{\partial U}{\partial R}\frac{\partial\tilde{I}}{\partial\varphi} + \nabla_\perp(\Delta^\dagger U)\cdot\nabla_\perp F \\
& +2\nabla_\perp\frac{\partial U}{\partial R}\cdot\nabla_\perp\frac{\partial F}{\partial R} + 2\nabla_\perp\frac{\partial U}{\partial Z}\cdot\nabla_\perp\frac{\partial F}{\partial Z}\} \\
& +\epsilon\nabla_\perp U\cdot\nabla_\perp\frac{\partial F}{\partial R} - \frac{\epsilon}{R}\frac{\partial F}{\partial Z}\frac{\partial U}{\partial Z} \\
& -\{\nabla_\perp(\Delta^*\chi)\cdot\nabla_\perp\psi + \nabla_\perp\chi\cdot\nabla_\perp(\Delta^*\psi) + 2\nabla_\perp\frac{\partial\chi}{\partial R}\cdot\nabla_\perp\frac{\partial\psi}{\partial R} + 2\nabla_\perp\frac{\partial\chi}{\partial Z}\cdot\nabla_\perp\frac{\partial\psi}{\partial Z}\} \\
& +\frac{2}{R^2}\frac{\partial\chi}{\partial R}\frac{\partial\psi}{\partial R} \\
& +\{\nabla_\perp(\Delta^*\chi)\times\nabla_\perp F\cdot\hat{\varphi} - \frac{1}{R}\nabla_\perp\chi\times\nabla_\perp(\frac{\partial\tilde{I}}{\partial\varphi})\cdot\hat{\varphi} - \frac{1}{R^2}\frac{\partial\tilde{I}}{\partial\varphi}\frac{\partial\chi}{\partial Z} \\
& +2\nabla_\perp\frac{\partial\chi}{\partial R}\times\nabla_\perp\frac{\partial F}{\partial R}\cdot\hat{\varphi} + 2\nabla_\perp\frac{\partial\chi}{\partial Z}\times\nabla_\perp\frac{\partial F}{\partial Z}\cdot\hat{\varphi}\} \\
& -\frac{1}{R}\nabla_\perp\chi\times\nabla_\perp\frac{\partial F}{\partial R}\cdot\hat{\varphi} - \frac{1}{R^2}\frac{\partial F}{\partial Z}\frac{\partial\chi}{\partial R} \\
& +\frac{\partial}{\partial\varphi}\nabla_\perp^2\Phi - \frac{\partial}{\partial\varphi}(\frac{1}{R}\frac{\partial\Phi}{\partial R}) \\
& +\Delta^*(\eta\Delta^*\psi) + \Delta^*(\frac{\eta}{R}\frac{\partial F}{\partial Z})
\end{aligned} \tag{13}$$

$$\begin{aligned}
\nabla_\perp^2\Phi = & \epsilon\nabla_\perp\tilde{I}\cdot\nabla_\perp U + I\Delta^\dagger U - \frac{I}{R}\frac{\partial U}{\partial R} + \frac{1}{R}\nabla_\perp\chi\times\nabla_\perp\tilde{I}\cdot\hat{\varphi} + \frac{R_0}{R^2}I\frac{\partial\chi}{\partial Z} \\
& -\frac{1}{R}\nabla_\perp v_\varphi\cdot\nabla_\perp\psi - \frac{v_\varphi}{R}\Delta^*\psi - \frac{1}{R}\nabla_\perp F\times\nabla_\perp v_\varphi\cdot\hat{\varphi} - \frac{v_\varphi}{R^2}\frac{\partial F}{\partial Z} \\
& -\eta\frac{1}{R^2}[\frac{\partial\tilde{I}}{\partial z} - \frac{1}{R}(\frac{\partial F'}{\partial Z} - \frac{\partial\psi'}{\partial R}) + \frac{\partial}{\partial\varphi}(RJ_\varphi)] \\
& +\frac{1}{R}(\nabla_\perp\eta\times\nabla_\perp\tilde{I})\cdot\hat{\varphi} - \frac{1}{R^2}(\nabla_\perp\eta\times\nabla_\perp F')\cdot\hat{\varphi} + \frac{1}{R^2}\nabla_\perp\eta\cdot\nabla_\perp\psi'
\end{aligned} \tag{14}$$

$$\begin{aligned}
\frac{\partial}{\partial t}\Delta^\dagger U = & \epsilon R[\nabla_\perp U\times\nabla_\perp(\Delta^\dagger U)]\cdot\hat{\varphi} - \nabla_\perp\chi\cdot\nabla_\perp(\Delta^\dagger U) - \frac{v_\varphi}{R}\frac{\partial}{\partial\varphi}\Delta^\dagger U \\
& -2\epsilon\Delta^\dagger U\frac{\partial U}{\partial Z} - \Delta^*\chi\Delta^\dagger U - \frac{2}{R}\frac{\partial\chi}{\partial R}\Delta^\dagger U \\
& -\frac{1}{R}\nabla_\perp v_\varphi\cdot\nabla_\perp(\frac{\partial U}{\partial\varphi}) + \frac{v_\varphi}{R^2}\frac{\partial}{\partial R}(\frac{\partial U}{\partial\varphi}) + \frac{2R_0}{R^2}v_\varphi\frac{\partial v_\varphi}{\partial Z} \\
& +\frac{R_0}{R^2}[\nabla_\perp v_\varphi\times\nabla_\perp(\frac{\partial\chi}{\partial\varphi})]\cdot\hat{\varphi} - \frac{R_0 v_\varphi}{R^3}\frac{\partial}{\partial Z}(\frac{\partial\chi}{\partial\varphi})
\end{aligned}$$

$$
\begin{aligned}
&-R_0\mathbf{B}\cdot\nabla(\frac{RJ_\varphi}{d})+R_0\mathbf{J}\cdot\nabla(\frac{R_0 I}{d})\\
&+\frac{2}{d}\frac{\partial p}{\partial Z}-\frac{R}{d^2}(\nabla_\perp d\times\nabla_\perp p)\cdot\hat{\varphi}. \qquad (15)\\
\frac{\partial v_\varphi}{\partial t}=&-R\epsilon(\nabla_\perp v_\varphi\times\nabla_\perp U)\cdot\hat{\varphi}-\nabla_\perp\chi\cdot\nabla_\perp v_\varphi-\frac{v_\varphi}{R}\frac{\partial v_\varphi}{\partial\varphi}\\
&+\frac{1}{d}(\nabla_\perp\tilde{I}\times\nabla_\perp\psi)\cdot\hat{\varphi}+\frac{1}{d}(\nabla_\perp\tilde{I}\cdot\nabla_\perp F)-\frac{1}{Rd}(\nabla_\perp F'\times\nabla_\perp\psi)\cdot\hat{\varphi}\\
&-\frac{1}{Rd}\nabla_\perp F'\cdot\nabla F-\frac{1}{Rd}\nabla_\perp\psi'\cdot\nabla_\perp\psi+\frac{1}{Rd}\hat{\varphi}\cdot(\nabla_\perp\psi'\times\nabla_\perp F)\\
&-\epsilon v_\varphi\frac{\partial U}{\partial Z}-\frac{v_\varphi}{R}\frac{\partial\chi}{\partial R}-\frac{\epsilon R}{d}\frac{\partial p}{\partial\varphi} \qquad (16)\\
\frac{\partial}{\partial t}\Delta^*\chi=&\,\epsilon^2R^2\nabla_\perp(\Delta^\dagger U)\cdot\nabla_\perp U+\epsilon^2R^2(\Delta^\dagger U)^2-\nabla_\perp(\frac{v_\varphi}{R})\cdot\nabla_\perp(\frac{\partial\chi}{\partial\varphi})-\frac{v_\varphi}{R}\Delta^*(\frac{\partial\chi}{\partial\varphi})\\
&+\frac{\partial}{\partial R}(\frac{v_\varphi^2}{R})-\frac{v_\varphi^2}{R^2}-\epsilon R[\Delta^\dagger U,\chi]-\epsilon[v_\varphi,\frac{\partial U}{\partial\varphi}]+\frac{\epsilon v_\varphi}{R}\frac{\partial}{\partial Z}(\frac{\partial U}{\partial\varphi})\\
&+R_0[\frac{I}{Rd},\frac{\partial\psi}{\partial\varphi}]+R_0\nabla_\perp(\frac{I}{Rd})\cdot\nabla_\perp(\frac{\partial F}{\partial\varphi})+\frac{R_0}{R}\frac{I}{d}\nabla_\perp^2(\frac{\partial F}{\partial\varphi})\\
&-\frac{R_0}{R^2}\frac{I}{d}(\frac{\partial^2\psi}{\partial\varphi\partial Z}+\frac{\partial^2 F}{\partial\varphi\partial R})\\
&-\nabla_\perp(\frac{C}{d})\cdot\nabla_\perp\psi-\frac{C}{d}\Delta^*\psi+[\frac{C}{d},F]-\frac{C}{Rd}\frac{\partial F}{\partial Z}\\
&-\epsilon R^2\nabla_\perp\frac{1}{d}\cdot\nabla_\perp p+4\epsilon\frac{p}{d}+4\epsilon\frac{R}{d}\frac{\partial p}{\partial R}-\frac{1}{d}\Delta^\dagger(\epsilon R^2p)\\
&-\Delta^*(\frac{v_\perp^2}{2})-\frac{R_0}{\epsilon}I\nabla_\perp\frac{1}{d}\cdot\nabla_\perp I+\frac{2R_0I}{Rd}\frac{\partial\tilde{I}}{\partial R}-\frac{1}{d}\Delta^\dagger(\frac{R_0^2I^2}{2}), \qquad (17)\\
\frac{\partial d}{\partial t}=&-d[\Delta^*\chi+\frac{1}{R}\frac{\partial v_\varphi}{\partial\varphi}]\\
&+R\epsilon\nabla_\perp U\times\nabla_\perp d\cdot\hat{\varphi}-\nabla_\perp\chi\cdot\nabla_\perp d-\frac{v_\varphi}{R}\frac{\partial d}{\partial\varphi} \qquad (18)\\
\frac{\partial p}{\partial t}=&\,R\epsilon\nabla_\perp U\times\nabla_\perp p\cdot\hat{\varphi}-\nabla_\perp\chi\cdot\nabla_\perp p-\frac{v_\varphi}{R}\frac{\partial\rho}{\partial\varphi}\\
&-\gamma p[\Delta^\star\chi+\frac{2}{R}\frac{\partial\chi}{\partial R}+2\epsilon\frac{\partial U}{\partial Z}+\frac{1}{R}\frac{\partial v_\varphi}{\partial\varphi}]. \qquad (19)
\end{aligned}
$$

Here all primes indicate toroidal derivative, and

$$
\nabla_\perp^2\equiv\frac{\partial^2}{\partial R^2}+\frac{\partial^2}{\partial Z^2},\;\;\Delta^\dagger\equiv\nabla_\perp^2+\frac{1}{R}\frac{\partial}{\partial R},\;\;\Delta^\star\equiv\nabla_\perp^2-\frac{1}{R}\frac{\partial}{\partial R}.
$$

The viscous terms are left out to conserve space.

3 Spatial and temporal discretization

There are altogether seven time evolution equations for $\tilde{I}, \Delta^\star\psi, \Delta^\dagger U, v_\varphi, \Delta^\star\chi, d$, and p. In addition, five Poisson equations are required to be inverted for the electric potential, flux and stream functions. These Poisson equations are strictly two dimensional, concern with poloidal (R, Z) planes only. For a general toroidal geometry can always be represented by a stack of shaped poloidal sections, we have adopted a mixed finite element and finite difference scheme. The shaped poloidal sections are treated by finite elements on unstructured grids, figure (3). The toroidal derivatives are calculated with fourth order finite difference.

There are three types of waves in the MHD model, the compressional Alfvén wave, the shear Alfvén wave, and the slow magnetosonic wave. The compressional wave in a toroidal device with strong toroidal field is stable, but poses the strictest constraints on the Courant-Friedrichs-Lewy (CFL) condition. The shear Alfvén wave is usually associated with the various instabilities, and is generally thought to be treated accurately to resolve the fast growing ideal MHD instabilities. One of the main benefit of our formulation is that the compressional wave is represented by a $\tilde{I}, \chi$, and p coupling. This coupling can be treated implicitly to overcome the fast compressional wave CFL constraint. Furthermore, this coupling involves only poloidal derivatives, so the matrix inversion problem is restricted to two dimensional (R, Z) plane. Taking advantage of these unique features of the equations, we have devised a time stepping scheme that treats only the compressional wave and dissipative terms implicitly, while treating the shear Alfvén dynamics explicitly for accuracy. We note that for the class of resistive instability (e.g. tearing modes) the growth rate is on the resistive time scale, which is many orders of magnitude slower that Alfvén wave transit time. It is then preferable to also treat the shear Alfvén dynamics implicitly. We are investigating to add an option to treat the poloidal shear Alfvén wave implicitly in the code. To deal with the irregularity in the mesh, we have find that a slightly dissipative scheme, like the third order Adam-Bashforth, does better than the variants of leapfrog scheme that was commonly used in MHD simulations.

4 Domain decomposition and PETSc solvers

Our spatial and temporal discretizations lead naturally to a three dimensional domain decomposition. Figure (2) shows a twenty-four processor decomposition for a Tokamak and a stellerator configuration. As shown in the illustration, a toroidal geometry is sliced into a set of poloidal planes, and a poloidal plane is further partitioned into equal area patches. A stack of poloidal patches (along the toroidal direction) is assigned to individual processors. Figure (3) gives another view of the flux surface aligned, unstructured, poloidal grids, and a twelve poloidal subdomain decomposition. The merit of this scheme include the flexibility of adjusting the aspect ratio of the subdomain, that the surface to volume ratio approaches that of a cubic, and excellent load balance.

The Poisson equations and the implicitness in time stepping introduce large sparse matrices to be inverted over a poloidal plane. This is addressed by iter-

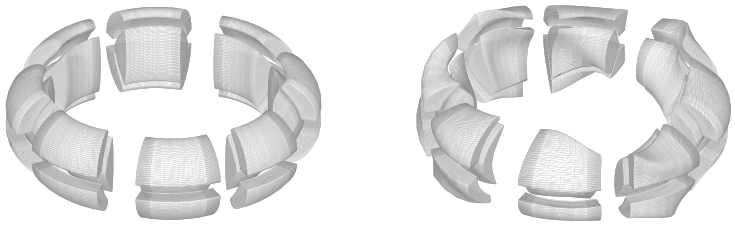

Figure 2. *Twenty four processor domain decomposition for a Tokamak (left) and a Stellerator (right).*

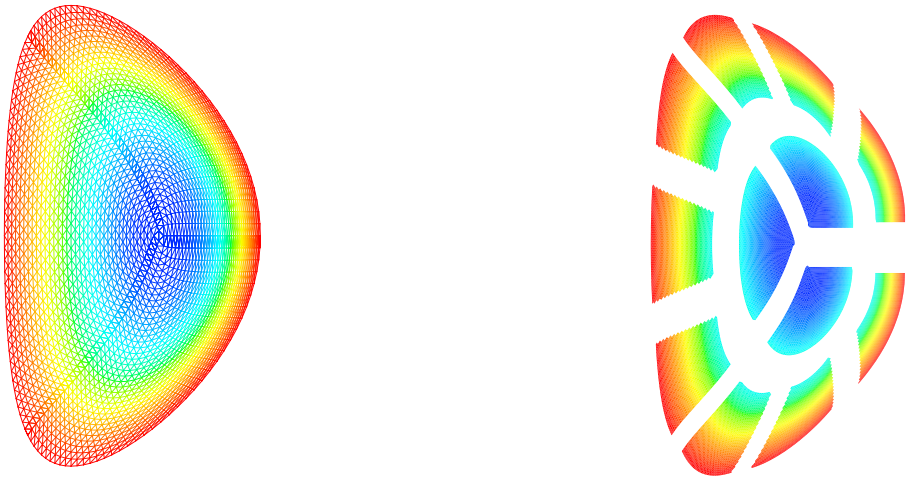

Figure 3. *Unstructured poloidal mesh and a finer poloidal decomposition.*

ative scheme with Krylov subspace acceleration. We have found that overlapped Schwarz method coupled with ILU provides adequate preconditioning for GMRES or BiCGSTAB. These functionalities are entirely provided by PETSc.

The parallel scalability of the design is satisfactory. In the toroidal direction, it is near ideal (linear speedup of fixed size problem as precessing elements increases) due to the time explicit scheme. In a poloidal plane where large sparse matrices are inverted, the degradation in the parallel scalability is gentle for a generously overlapped Schwartz preconditioning scheme[4]. The overall scalability of the code

can be optimized by varying the aspect ratio of a sub-partition. We note that the design of the mesh and domain decomposition has been devised to accommodate future coupling with particle simulations [5].

PETSc has proven to be ideal for enabling a rapid numerical implementation of this physics simulation model on massively parallel computers. The global MPI communicator is partitioned and recombined to form intersecting local poloidal and toroidal communicators. The ranks of each sub-partition in the local poloidal and toroidal communicators serve as a coordinate in a two dimensional index space. Parallel data structure like array and matrix are implemented as PETSc Vec and Mat [6] over local poloidal communicator to enable access to PETSc linear solvers (SLES). The toroidal ghost zones are explicitly implemented in the code since no sparse matrix solve involving toroidal coupling is required. The exchange of toroidal information is greatly simplified by the formation of local toroidal communicator.

The algebraic overlapped Schwarz preconditioner is a critical PETSc functionality for our simulation. We have found that without overlapping, the iterative scheme seldom converges. Rapid convergence is achieved if moderate (2-5 grid points) overlapping is employed. The algebraic implementation of this scheme in PETSc removes the cumbersome and error-prone task of constructing new parallel data layout associated with a variable ghost zone.

5 MHD activity in a TOKAMAK

Our parallel MHD code has been undergoing a physics validation and benchmarking process. These include axisymmetric equilibrium check and perturbative calculations of global MHD modes such as toroidal Alfvén eigenmode (TAE), kink, ballooning, and tearing modes. Here we will show two examples, one with a stable TAE mode, and the other with an ideally ($\eta = 0$) unstable ($n = 1, m = 1$) kink, where n, m are the toroidal and poloidal mode numbers.

It is known that in ideal MHD with uniform field, the shear Alfvén wave typically has a continuous spectra[7]. In a toroidal plasma, the toroidal magnetic field is non-uniform over a magnetic surface and causes coupling of different poloidal harmonics. This can break up the shear Alfvén continuous spectrum and create discrete low n shear Alfvén eigenmodes inside the continuum gaps[8]. The ideal low-n TAE is stable, and would decay if dissipation is introduced (finite resistivity and viscosity). Due to the global nature of this mode (low n, m and radially extended), it decays slower than the background noise. As the result, an initial perturbation quickly settles down on the primary TAE. The energy in the perturbation, though decaying due to dissipation, beats on the TAE eigenfrequency, figure (4). The mode structure of an $n = 1$ TAE is also shown in figure (4). One of the motivations of this benchmark was to verify the time unit normalization of the code implementation.

When the safety factor on the magnetic axis q_0 drops below unity, there is a $q = 1$ magnetic surface inside the Tokamak. The $n = 1, m = 2$ component tends to stabilize the $n = 1, m = 1$ via poloidal coupling in a torus. But it becomes insufficient once the poloidal beta, defined as the average pressure over the poloidal

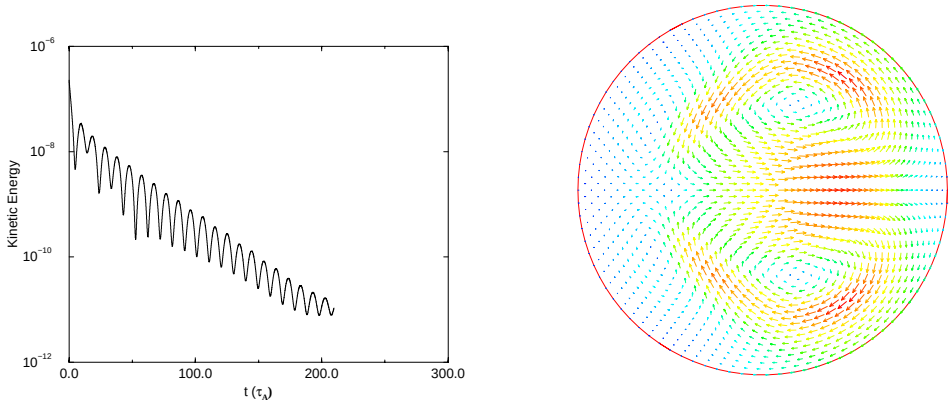

Figure 4. *Decaying kinetic energy of the MHD perturbation oscillates with the TAE eigenfrequency (left) and mode structure of this $n = 1$ TAE (right).*

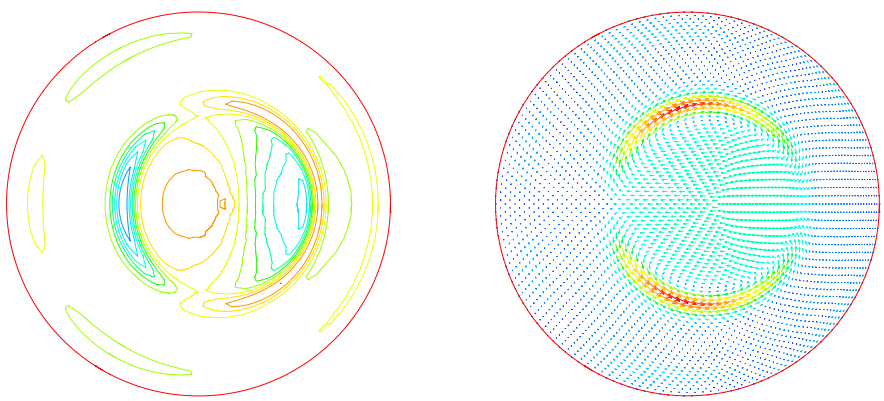

Figure 5. *Mode structure of an internal kink at $\varphi = \pi/2$ plane: perturbed RJ_φ (left) and poloidal flow (right).*

field strength squared, exceeds a modest value[9]. Figure (5) shows the mode structure of such a $(1, 1)$ kink. In the framework of resistive MHD, a small but finite resistivity increases the growth rate while finite viscosity slowing down the mode. The convergence to the ideal limit is investigated by varying the resistivity while maintaining a comparable magnetic Prandtl number ($Pr \equiv \nu/\eta$), and by varying the viscosity at a fixed small resistivity ($\eta = 10^{-6}$), figure (6). In either case, the growth rates of the mode are observed to approach the ideal limit ($\eta = \nu = 0$) as

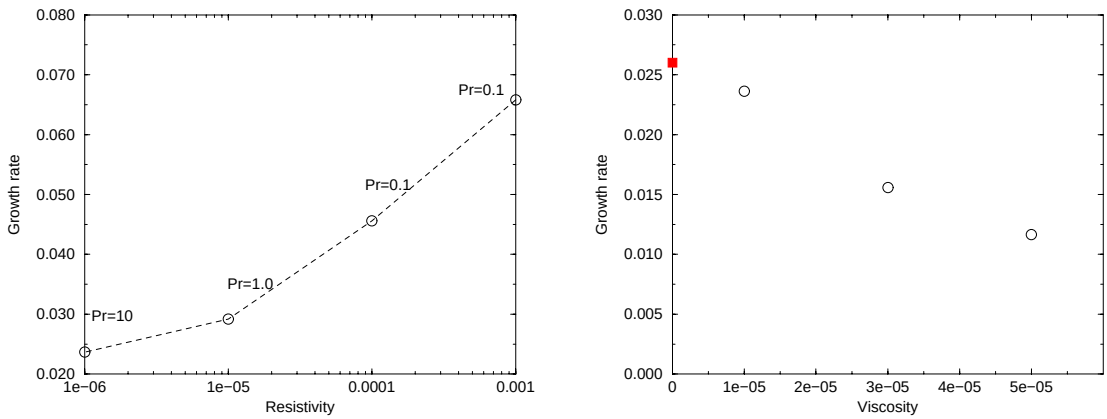

Figure 6. *Growth rate approaches ideal limits (red square) as resistivity and viscosity are reduced. The η is fixed at 10^{-6} in the second plot.*

calculated by a linear stability code NOVA[10].

6 Flux surface quality of stellerator equilibriums

The main subtlety for non-axisymmetric geometry is the implementation of boundary conditions in our mixed field-current representation of the MHD equations. This is resolved by a new formulation based on generalized Ohm's law[11]. The three dimensional capability of the code can be demonstrated on stellerator equilibrium reconstruction which has a non-axisymmetric magnetic field. The advantage of a stellerator is its potential for disruption-free steady state operation. But closed flux surface, another critical property for good confinement, is known to be fragile in a general three dimensional field. In practice, an equilibrium configuration is numerically found through variational principle by writing the magnetic field in a form that imposes good flux surfaces, such as the VMEC code [12]. This weak solution to the force balance equation $\mathbf{J} \times \mathbf{B} = \nabla p$ is equivalent to assuming a perfectly conducting plasma. Magnetic perturbation theory tells us that this perfectly conducting plasma preserves closed flux surfaces by running a singular current that cancels the external resonant perturbation at the resonant magnetic surface. However, singular current is difficult to rigorously retain in numerical solution, and it will decay away in a realistic resistive plasma and hence allow island opening and flux surface breakup. It was conjectured that by reconstructing the magnetic field from VMEC current with a general magnetic field representation, the effect of the absence of singular cancellation current can be assessed.

Figures (7,8) show Poincaré sections of the magnetic field on the $\varphi = 0$ poloidal plane for two national compact stellerator experiment (NCSX) candidate configurations, the c82 and li383. The magnetic field is reconstructed from the VMEC cal-

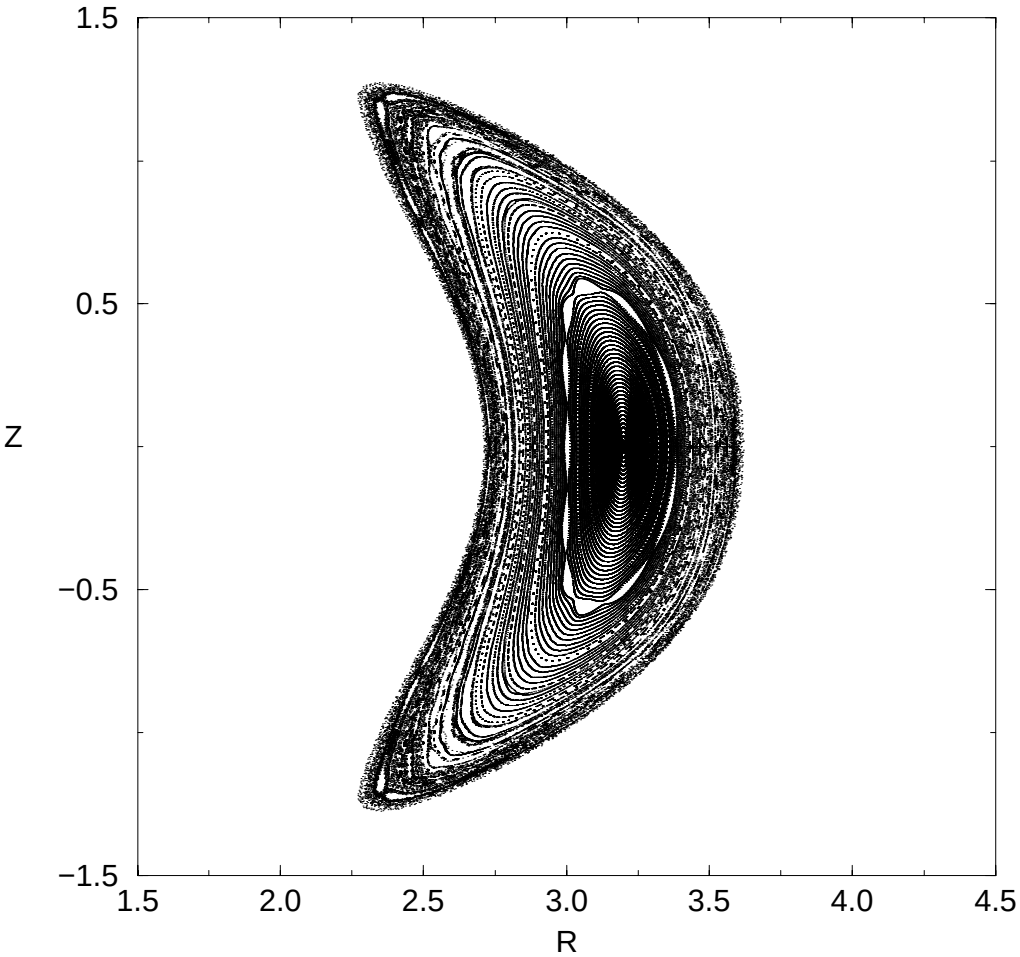

Figure 7. *Poincaré plot of NCSX c82 candidate configuration at* $\varphi = 0$.

culated B_φ and j_φ. From VMEC $B_\varphi, \tilde{I}$ is calculated by its definition, equation (9). One then finds F by solving equation (12). With F and VMEC toroidal current j_φ, the flux function ψ is calculated from equation (10). The Poincaré plot is then obtained by integrating the field line trajectories and locating its intersection with the $\varphi = 0$ plane. Over one million grids are employed to cover one period of the three-period c82 in figure (7). The prominent features of c82 reconstructed field are

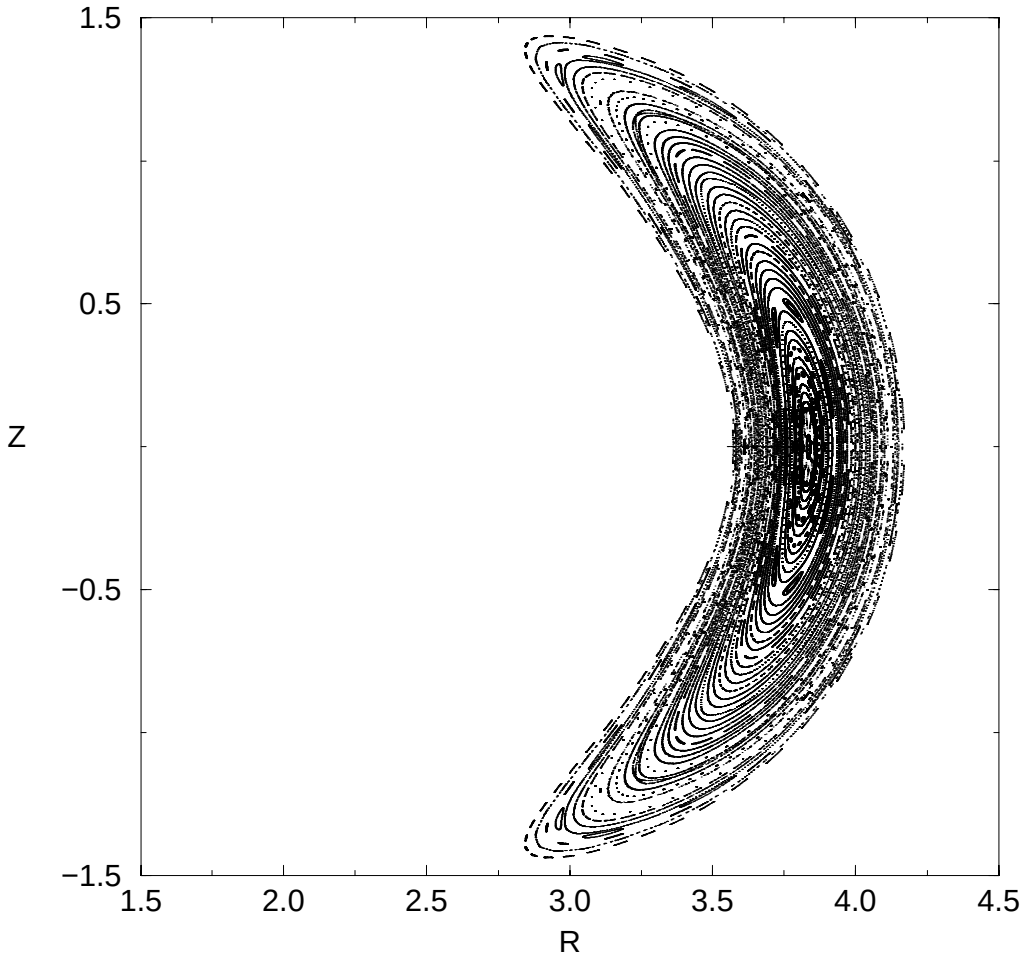

Figure 8. *Poincaré plot of NCSX li383 candidate configuration at* $\varphi = 0$.

the presence of large $(n = 3, m = 11)$ island chain, and stochasticity on the edge. In contrast, with two million grids covering one period of the period three li383, we find much better flux surface properties, particularly on the edge. There are island chains at the primary resonances $(n = 3, m = 5)$ and $(n = 3, m = 7)$, and higher order resonances $(n = 15, m = 23)$ and $(n = 9, m = 14)$.

Bibliography

[1] D. Biskamp, *Nonlinear magnetohydrodynamics*, Cambridge University Press, (1993).

[2] S. Balay, W. D. Gropp, L. C. McInnes, and B. F. Smith, *Efficient Management of Parallelism in Object Oriented Numerical Software Libraries*, in Modern Software Tools in Scientific Computing, edited by E. Arge and A. M. Bruaset and H. P. Langtangen, Birkhauser Press (1997), pp.163–202.

[3] R. Izzo, D. A. Monticello, J. Delucia, W. Park, C. M. Ryu, *Reduced equations for finite beta-tearing modes in Tokamak*, Physics of Fluids, 28 (1985), pp. 903–911.

[4] D. E. Keyes, D. K. Kaushik, and B. F. Smith, *Prospects for CFD on petaflops systems*, ICASE Report No. 97-73, (1997).

[5] W. Park, E. V. Belova, G. Y. Fu, X. Z. Tang, H. R. Strauss, and L. E. Sugiyama, *Plasma simulation studies using multilevel physics models*, Physics of Plasmas, 6 (1999), pp.1796–1803.

[6] S. Balay, W. D. Gropp, L. C. McInnes, and B. F. Smith, *PETSc 2.0 Users Manual*, ANL-95/11 - Revision 2.0.29, Argonne National Laboratory, 2000.

[7] J. P. Freidberg, *Ideal magnetohydrodynamics*, Plenum Press, New York (1987).

[8] C. Z. Cheng and M. S. Chance, *Low-n shear Alfvén spectra in axisymmetric toroidal plasmas*, Physics of Fluids, 29 (1986), pp.3695–3701.

[9] M. N. Bussac, R. Pellat, D. Edery, and J. L. Soulé, *Internal kink modes in a toroidal plasma with circular cross section*, Phys. Rev. Lett., 35 (1975) pp.1638–1641.

[10] C. Z. Cheng and M. S. Chance, *NOVA - A nonvariational code for solving the MHD stability of axisymmetrical toroidal plasmas*, J. Comp. Physics, 71 (1987), pp.124–146.

[11] X. Z. Tang, *On the ideal boundary condition in a general toroidal geometry for a mixed magnetic field representation*, PPPL report (2000).

[12] S. P. Hirshman, W.I. van Rij, and P. Merkel, *Three-dimensional free boundary calculations using spectral Green's function method*, Computer Physics Communications, 43 (1986) pp.143–155.

[13] A. Reiman, et al, *Recent advances in the design of quasi-axisymmetric stellerator plasma configurations*, to appear in Physics of Plasmas (2001).